ACS APPLIED ELECTRONIC MATERIALS

pubs.acs.org/acsaelm

Article

Eco-Friendly Energy Storage and Energy Harvesting Devices Fabricated by Direct Laser Writing of Chitosan-Lignin-Boric Acid Substrates

Published as part of ACS Applied Electronic Materials special issue "Sustainable Development of Printed Electronics: From Materials Processing to Devices Implementation".

Jahidul Islam,[#] Rafael Resende Assis Silva,[#] Alessandra Imbrogno, Caio G. Otoni, Rodrigo Martins, Luiz Henrique Capparelli Mattoso,* Aidan J. Quinn, and Daniela Iacopino*

Cite This: *ACS Appl. Electron. Mater.* 2025, 7, 4801−4813

Read Online

ACCESS | Metrics & More | Article Recommendations | Supporting Information

ABSTRACT: Eco-friendly supercapacitor (SC) and triboelectric nanogenerator (TENG) devices were assembled using laser-induced graphene (LIG) electrodes fabricated by direct laser writing of chitosan-lignin-boric acid films. A simple one-step laser irradiation was used to convert the chitosan-based films into 3D, interlinked, and electrically conductive LIG electrode materials. Assembled SCs displayed specific areal capacitances up to 21.4 mF/cm^2 at a current density of 0.05 mA/cm^2 and 68% capacitance retention for >10,000 charge/discharge cycles. When charged by a commercial solar cell, the SC could power a digital thermo-hygrometer, an electronic stopwatch and a calculator, showing potential for real applications. Single-electrode TENG (SE-TENG) devices were also assembled using PDMS as the dielectric layer. The TENGs displayed an open-circuit voltage of 13.3 V, a short-circuit current of 1.7 μA, and stability over 10,000 cycles. The TENG could charge commercial SCs of 0.1 and 1 μF capacitance in less than 60 s. This work demonstrates the suitability of sustainable materials as feedstock constituents for the generation of LIG electrodes and opens the door to the large-scale production of cost-effective electrode materials for "green" wearable electronic applications.

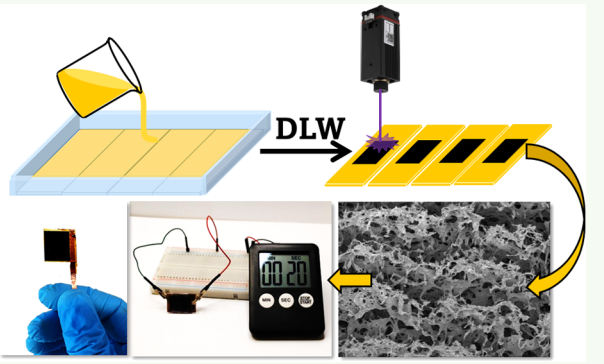

KEYWORDS: *laser-induced graphene, sustainable materials, supercapacitor, triboelectric nanogenerator, biodegradable device, wearable electronics, energy harvesting*

INTRODUCTION

Wearable sensors have gained much attention in recent decades for their applications in health,[1,2] sport,[3] fitness, and wellbeing,[4] enabling the monitoring of biomarkers and the transition from centralized to personal, point-of-care monitoring.[5] The rapid technological development and high demand for such wearable devices require the urgent development of lightweight, flexible, and robust power systems. Supercapacitors (SCs) are increasingly used in wearable electronics as an alternative to traditional batteries, as they combine lightweight and flexibility with high-power density, fast charging/discharging ability, and long cycle life.[6−9] A possible alternative strategy to reduce weight and volume in wearable designs is the incorporation of energy harvesting devices to achieve self-powering capabilities.[10,11] Triboelectric nanogenerators (TENGs) are devices capable of harvesting and converting mechanical energy from various stimuli—solid−solid, liquid−solid, and gas−solid—into electricity, generating high AC voltage through the combined effects of contact electrification and electrostatic induction.[12−15] Due to the low cost of materials involved, simplicity of operation, versatility of configuration, and wide range of applications, TENGs are being increasingly considered for wearable power supplies and versatile self-powered sensing applications.[16]

Recently, direct laser writing (DLW) has emerged as a high-throughput and eco-friendly manufacturing technique for the realization of energy storage[17−19] and energy harvesting[20−22] devices. In this method, low-cost hobbyist lasers are used to "write" laser-induced graphene (LIG) conductive patterns on

Received: January 31, 2025
Revised: May 10, 2025
Accepted: May 12, 2025
Published: May 16, 2025

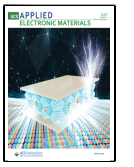

flexible polymer substrates without the use of templates or chemicals. The obtained LIG structures exhibit high surface area, high density of defects, and low sheet resistance (R_{sh} < 50 ohm/sq), making LIG an ideal electrode material for energy applications. For example, the application of DLW methods to commercial polyimide substrates (Kapton tape) has led to the development of microsupercapacitors with excellent capacitive behavior and showing areal capacitances up to 16.5 mF/cm^2.[17−19] LIG has also been used in energy harvesting applications. Stanford et al. fabricated LIG-TENGs on polyimide and cork substrates obtaining open-circuit voltages >3.5 kV and peak power >8 mW.[20] Yang et al. used polyimide paper to realize novel foldable and stackable TENGs, also displaying tailorable performance and enhanced versatility.[22] Shrestha et al. developed the first example of an SC power cell (SPC) in which the energy generated from a TENG device was stored in an SC without power management or rectifier circuits via a tribo-electrochemical mechanism. The self-charging SPC combined TENG and SPC into a single integrated device, with TENG generating 2.5 mW power, which successfully charged the SPC to a maximum voltage of 210 mV within 9 s.[23]

In parallel to the above technological advances, new efforts are nowadays concentrating on embedding abundant, natural, or renewable constituent materials into energy devices toward development of green wearable technologies with reduced environmental impact. Interestingly, it has been recently demonstrated that natural and abundant precursors can be used as feedstock materials for the production of "green" LIG, making this process amenable to the fabrication of biodegradable electronic platforms.[24−26] For example, our group and others have investigated the merit of sustainable paper, lignin-enriched paper, and cork for the production of LIG SC electrodes, reaching impressive areal capacitance (up to 10 mF/cm^2), power (4 μW cm^{-2} at 0.01 mA/cm^2), and energy (~4 μW cm^{-2} and ~0.77 μWh/cm^2 at 0.01 mA/cm^2) densities.[27,28] Chi et al. have designed a rice-based TENG able to produce 244 V with 6 μA of short-circuit current and 37 μW/cm^2 of power density.[29] Saqib et al. have fabricated a TENG from waste peanut shells achieving 910 V open-circuit voltage and 104.5 μA short-circuit current with 12 mW of peak instantaneous power.[30] Singh et al. also have used waste from fish fins as well as other biomaterials combinations (egg shell membrane, dog hairs, tree cotton) to fabricate TENGs, achieving 130 V, with 1.1 μA measured across a 1 MΩ resistor.[31]

In this work, "green" LIG electrodes were fabricated by one-step DLW of flexible chitosan-lignin-boric acid films. The electrodes displayed the typical high surface area of LIG materials obtained from conventional polyimide and were used to assemble energy storage and harvesting units. The SCs showed impressive areal capacitance of 15.2 mF/cm^2 at 0.1 mA/cm^2 and good stability and cyclability, with retention of 68% of the initial capacitance after >10,000 charge/discharge cycles. When assembled in series and charged with a commercial solar cell, the SCs were able to power an electronic thermo-hygrometer, a stopwatch and a calulator, showing promising real-world application capabilities. Single-electrode TENG devices were also fabricated, which showed open-circuit voltages of 3.7−13.3 V for 30−60 N applied forces. The capability of TENGs to charge commercial supercapacitors was also shown, toward demonstration of practical applications.

METHODS

Materials. Chitosan powder (CS, medium molecular weight), glycerol (99.5%), lignin alkali (LIGN, 95% pure), acetic acid (50%), boric acid (BA) powder (H_3BO_3, 99.5%), poly(vinyl alcohol) (PVA, M_w 89,000−98,000), and sulfuric acid (96%) were purchased from Sigma-Aldrich. Polydimethylsiloxane (PDMS) base and curing agent at a 10:1 ratio (Dowsil 184 Sylgard) were purchased from Farnell Ireland. All of the chemicals were used without further purification or modification. All solutions were prepared using deionized (DI) Milli-Q water (resistivity ~18.2 MΩ/cm).

Preparation of Chitosan-Lignin-Boric Acid (CS-LIGN-BA) Substrate. Chitosan (2 g), glycerol (2 mL), and lignin alkali powder (0.3 g) were dissolved in 100 mL of an aqueous solution of acetic acid (1%) and stirred for 1 h. Different amounts of BA, equivalent to 1−11% relative to chitosan weight, were added to the solution, which was stirred for 24 h (Table S1). The resulting mixtures were poured on polyethylene terephthalate (PET) sheets in a plastic tray and dried for 48 h at room temperature to get a 200 μm thick flexible CS-LIGN-BA film on PET.

LIG Fabrication. LIG electrodes were fabricated via laser irradiation using a K5 compact desktop mini laser engraving machine equipped with a 450 nm wavelength laser and a 3000 mW power source. To ensure stability during laser processing, PET films were secured onto a glass slide by using double-sided tape. LIG patterns were laser-written onto CS-LIGN-BA films with optimized laser power and depth settings, determined through a Design of Experiments (DoE) approach using Design Expert 11 software. A randomized parameter set was employed to enhance the LIG production efficiency.

Fabrication of Energy Storage and Harvesting Devices. For the fabrication of SCs, a sandwich configuration was designed by using LIG square (1 cm^2) electrodes. A PVA/H_2SO_4 electrolyte solution was prepared by stirring 1 g of PVA and 1 mL of H_2SO_4 together in 10 mL of deionized water at 80 °C overnight. A sintered polypropylene separator with a thickness of 100 μm was placed between two LIG electrodes filled with a PVA/H^+ electrolyte solution. The outside edges of the LIG electrodes were painted with conductive silver paint to ensure stable electrical connections to the potentiostat. Prior to electrochemical measurements, the SC sandwich device was placed in a tightly screwed aluminum holder and stored overnight in a vacuum desiccator to remove any excess moisture and ensure electrolyte penetration into the porous electrodes.

SE-TENG devices were fabricated using LIG as electrodes and poly(dimethylsiloxane) (PDMS) as the triboelectric layer. The PDMS layer was prepared by mixing the silicone elastomer precursor with the curing agent (Sylgard 184) in a 10:1 volume ratio. After mixing throughly, the PDMS mixture was vacuum degassed for 1 h to remove air bubbles. The degassed PDMS was then spin-coated onto a square-shaped LIG surface (3.8 cm^2) maintaining a constant acceleration speed of 200 rpm for 60 s. After deposition, the PDMS layer was further vacuum degassed for 1 h to ensure uniformity and eliminate any remaining bubbles. The layer was then cured at 80 °C for 1 h, resulting in an average thickness of approximately 225 μm, as measured with a Mitutoyo external micrometer. To facilitate electrical measurements, copper tape was attached to the LIG surface, serving as the connection point for electrical wiring.

Characterization. The electrical conductivity of the fabricated LIG structures was determined through Transfer Line Measurements (TLM). Transfer line structures (16 × 4 mm) were contacted directly by using a probe station (Wentworth Laboratories PML 8000) at known separation lengths. Potential−current sweeps (−0.1 to 0.1 V, 10 mV step) were recorded using a parameter analyzer (Agilent 5270B). Surface morphology and elemental analysis were performed using scanning electron microscopy (SEM) and energy-dispersive X-ray spectroscopy (EDX) with a Zeiss Supra 40, equipped with an Oxford X-Max 50 detector, operating at an accelerating voltage of 10 kV. Samples were coated with an ~10 nm film of AuPd (90%Au, 10% Pd) prior to imaging. X-ray photoelectron spectroscopy (XPS) measurements were conducted in a vacuum transfer module using a

https://doi.org/10.1021/acsaelm.5c00234
ACS Appl. Electron. Mater. 2025, 7, 4801−4813

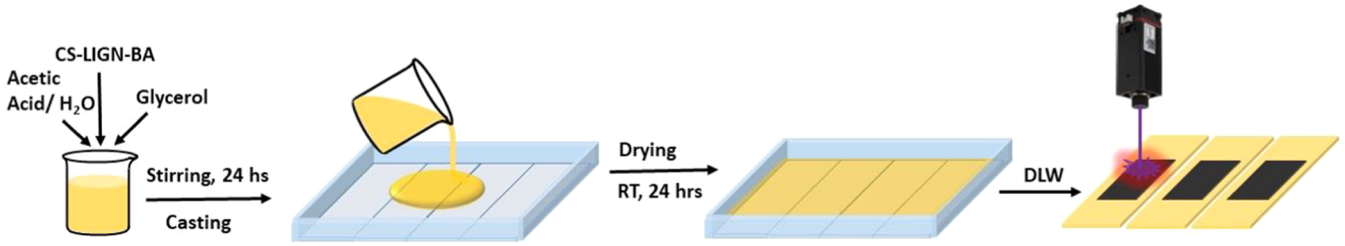

Figure 1. Schematic process for the preparation of CS-LIGN-BA substrates by casting aqueous CS-LIGN solutions with 3−11 wt % of BA into PET substrates, followed by LIG fabrication by DLW.

K-α (Thermo Scientific) 180° double-focusing hemispherical analyzer with 128-channel detector and Al Kα microfocused monochromator with an excitation energy (hν = 1486 eV) and X-ray spot size of 300 μm. The electron energy analyzer operated with a constant pass energy of 50 eV for high-resolution (HR) spectra and 200 eV for the survey spectra. A dwell time of 50 ms was used for HR spectra and 10 ms for survey spectra along with 10 and 20 scans, respectively. Raman investigation was performed with a Horiba-XPlora equipped with a 70 mW 532 nm laser diode. Spectra were acquired at a laser power of 10% and a 30 s acquisition time. X-ray diffraction (XRD) measurements were carried out by scanning from 4 to 70° (2θ) with a Shimadzu XRD-6000 X-ray diffractometer at a rate of 1°min^{-1}. Thermogravimetry (TG) was conducted by using a QG50 TG analyzer from TA Instruments (USA) under a nitrogen atmosphere at a flow rate of 40 mL/min. Samples of 10 mg were placed in platinum crucibles and heated from 25 to 800 °C at a rate of 10 °C/min.

To investigate the electrochemical performance of the SC devices, cyclic voltammetry (*CV*), galvanostatic charge−discharge (GCD), and electrochemical impedance spectroscopy (EIS) measurements were performed with a multichannel (Autolab PGSTAT M204) electrochemical workstation at ambient condition. The specific areal capacitance (C_A) was calculated from GCD curves using the standard eq 1,[27]

$$C_A = \frac{I}{S \times (dV/dt)} \quad (1)$$

where I denotes the constant discharge current, S is the total active area of positive and negative electrodes in cm^2, and dV/dt represents the slope of the discharge as obtained from the charge−discharge curve. EIS spectra of all LIG supercapacitor devices were obtained at open-circuit potential (OCP) in the range −0.047 to +0.045, in the frequency ranging from 10 kHz to 0.01 Hz using an AC amplitude of 10 mV.

Open-circuit electrical voltages (V_{OC}) generated from the constructed SE-TENG device were measured by varying the applied mechanical forces (30 to 60 N) and frequencies (2 to 10 Hz). The short-circuit current (I_{SC}) output was measured under varying forces (30 and 60 N) at a fixed frequency of 2 Hz. The TENGs were connected to an external circuit for measurements, and the data was collected using an oscilloscope (Tektronix TBS1000C). In all cases, the triboelectric layer matched the area of the LIG electrode, and the V_{OC} results were normalized based on the TENG contact volume. Mechanical drive was generated by using a custom-made device. The TENG's electrical output stability was evaluated by monitoring V_{OC} over 10,000 cycles at 50 N and 2 Hz. Instantaneous power was calculated by using $P = V^2R^{-1}$ from the data obtained from voltage measurements in the corresponding load resistance (R). V_{OC} and I_{SC} output under activation at 50 N and 2 Hz across different resistance ranges (0.1 to 200 MΩ) was evaluated. Then, instantaneous power was plotted as a function of time, and power density was calculated by dividing the power by the sample contact area. The surface charge density was obtained following the method proposed by Germane,[32] in which the surface charge Q (nC) was determined from the measured current peaks using eq 2:

$$Q = \int i dt \quad (2)$$

where i is the instantaneous current (nA) and dt is the time differential (s). Integration was done for the highest and lowest peaks corresponding to the separation stage.

RESULTS AND DISCUSSION

Figure 1 schematically illustrates the fabrication of CS-LIGN-BA substrates along with the process of LIG fabrication by one-step visible laser irradiation.

Laser writing conditions were optimized for LIG production using CS-LIGN-BA substrates with 5% wt. BA, as this concentration was found to be optimum in previously fabricated LIG electrodes from polyimide substrates.[33,34] DLW was carried out by using a DoE approach, whereby laser power (LP) and laser depth (LD) were systematically changed between 30−80% and 40−80%, respectively, aiming at obtaining LIG materials with the lowest values of sheet resistance (R_{SH}). Figure 2a shows the DoE graph where the values of R_{SH} obtained for LIG written with different LP-LD combinations are shown as color density (blue to green

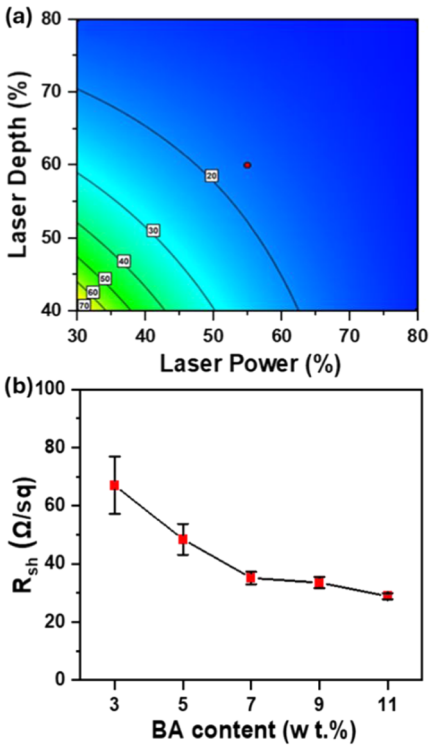

Figure 2. (a) Response surface design of experiment (DoE-RS) model output for R_{SH} vs various LP-LD combinations; (b) R_{SH} of LIG structures obtained by laser writing (55−60 LP-LD) of CS-LIGN-BA films with different BA contents (wt %).

https://doi.org/10.1021/acsaelm.5c00234
ACS Appl. Electron. Mater. 2025, 7, 4801−4813

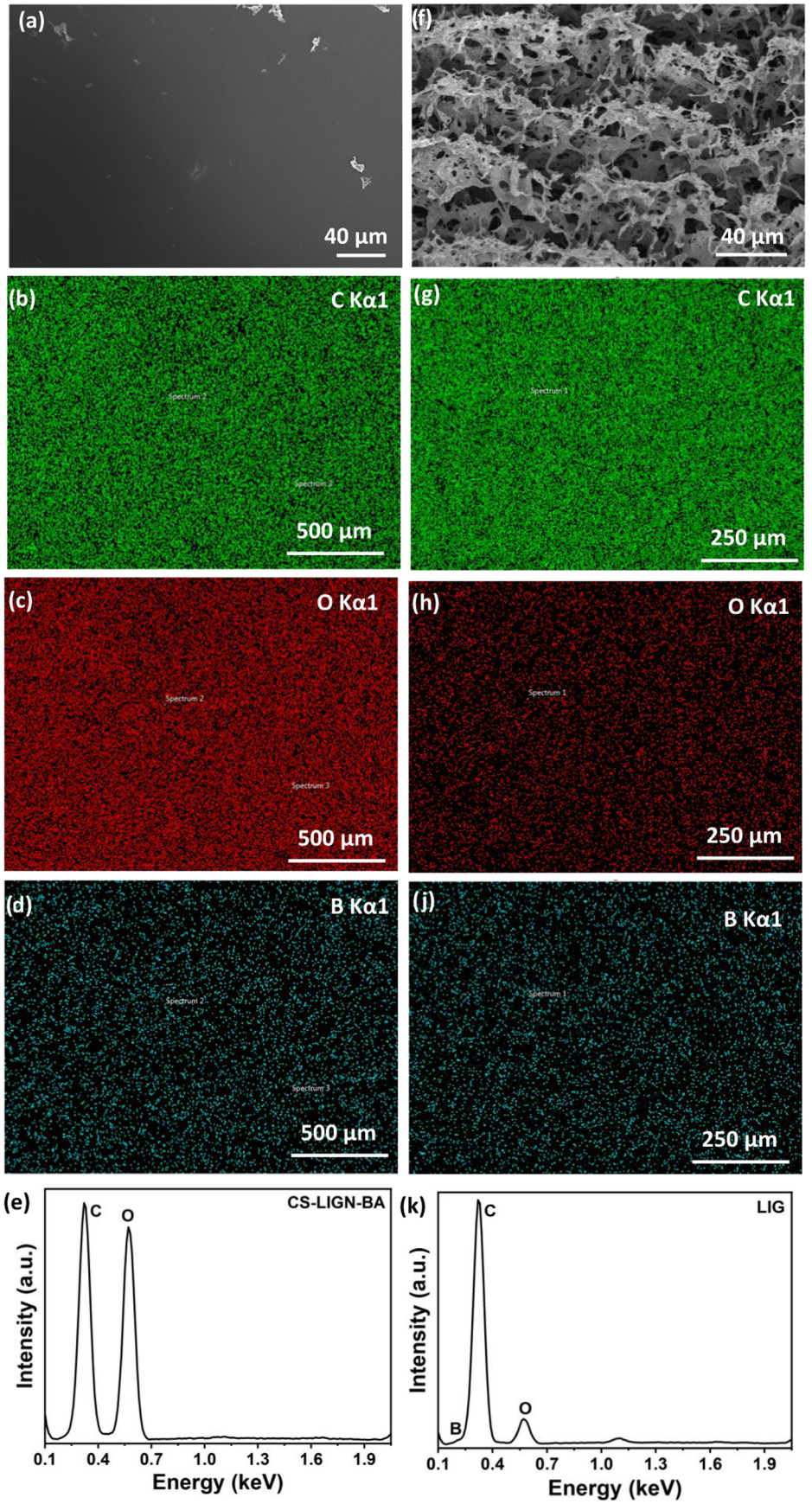

Figure 3. (a) SEM image of pristine CS-LIGN-BA substrate. SEM-EDS mapping of CS-LIGN-BA substrate, showing distribution of (b) C, (c) O, and (d) B. (e) Representative SEM-EDS graph for CS-LIGN-BA. (f) SEM image of LIG. SEM-EDS mapping of LIG, showing distribution of (g) C, (h) O, and (j) B. (k) Representative SEM-EDS graph for LIG on CS-LIGN-BA.

https://doi.org/10.1021/acsaelm.5c00234
ACS Appl. Electron. Mater. 2025, 7, 4801−4813

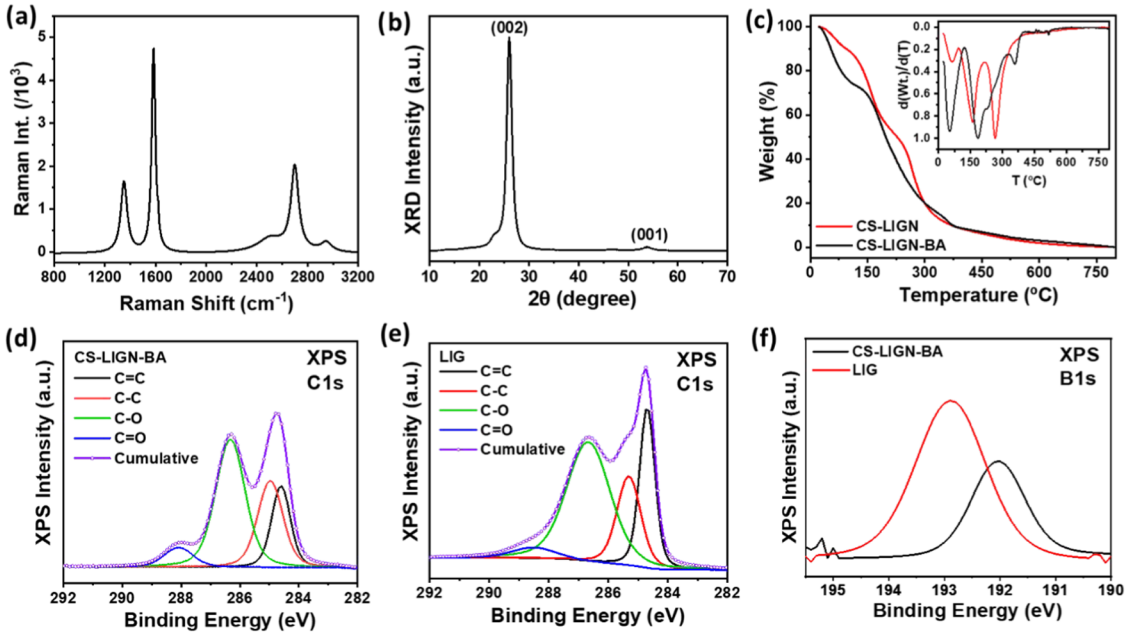

Figure 4. (a) Raman spectrum of LIG; (b) XRD pattern of LIG; (c) TGA profiles of CS-LIGN and CS-LIGN-BA substrates; (d) XPS C 1s spectra of pristine CS-LIGN-BA films, (e) XPS C 1s spectra of LIG, and (f) XPS B 1s spectra of CS-LIGN-BA and LIG.

equivalent to low to high). The calculation showed that the LP-LD combination of 30−40 was the minimum required parameter setting for the successful conversion of CS-LIGN-BA into LIG. However, these experimental conditions led to the formation of LIG structures showing a high average R_{SH} of ∼121 Ω/sq. In contrast, the lowest average R_{SH} value (∼12 Ω/sq) was found for the LP-LD combination of 80−80. However, LIG structures formed under these experimental conditions were highly brittle. Therefore, an LP-LD 55−60 combination was chosen for further study, as the obtained LIG structures showed an acceptably low average R_{SH} of 33 Ω/sq while maintaining their flexibility. After optimization of the laser writing parameters, the contribution of BA was investigated, with the purpose of choosing the BA concentration (wt %) leading to the formation of LIG structures with the lowest R_{SH} values. Figure 2b shows that the average R_{SH} of LIG decreased as the BA content in the CS-LIGN mixture increased until reaching a plateau at BA concentrations of 9% and higher. Based on this trend, 9% BA was selected for synthesizing subsequent substrates for LIG production, achieving a dry mass loading of CS-LIGN-BA on PET equivalent to 21.36 mg/cm^2. BA concentrations below 3% were not included, as graphitization did not occur. Furthermore, for BA concentrations above 3%, graphitization was observed even in the absence of LIGN. However, the inclusion of LIGN led to LIG structures of lower R_{SH} values (33 Ω/sq with LIGN vs 75 Ω/sq with no LIGN) and enhanced the overall substrate hydrophobicity, resulting in SC and TENG devices of greater electrochemical performance and mechanical/chemical stability.

Figure 3 shows SEM images associated with the graphitization of the CS-LIGN-BA substrates. The pristine film (Figure 3a) showed a smooth surface with some residual wrinkles arising from the drying process. Figure 3b−d shows the SEM-EDS mapping displaying homogeneous distribution of C, O, and B in the film. A representative EDS spectrum is shown in Figure 3e, with atomic percentages of C, O, and B equal to 50.0, 42.8, and 7.3 wt %, respectively. The SEM image of LIG (Figure 3f) illustrates a clear transition from a smooth morphology to a significantly corrugated and elevated morphology upon graphitization and LIG formation. The image showed quite clearly the formation of parallel linear LIG structures about 30 μm wide, associated with the raster scanning movement of the laser during the writing process. The laser-written area showed the typical "exploded" LIG morphology, characterized by high density of microholes and defects and displaying high surface area and porosity. This morphology resembled closely the morphology of LIG and green-LIG structures previously obtained by laser writing of polyimide and biomaterials, respectively.[26,27,35] Figure 3g−k shows SEM-EDS mapping and atomic percentages of C, O, and B in the LIG materials. Following laser treatment, the C content increased to 82 wt %, indicating the occurrence of graphitization; the O content decreased to 9.3 wt %, and the B content showed a slight increase (8.7 wt %), indicating incorporation of boron into the LIG structure. The cross-sectional SEM micrograph revealed an approximate CS-LIGN-BA thickness of ∼200 μm (Figure S1a) and an LIG thickness ranging from 100 to 157 μm (Figure S1b), consistent with reported values for chitosan-based derivatives.[36] The high LIG thickness played a crucial role in modulating the lateral electron pathways and charge transfer routes, contributing to the observed low sheet resistance (∼33 Ω/sq). The SEM-EDS mapping of the cross-sectioned LIG (Figure S1c,d) homogeneous atomic distribution of C and B throughout the material vertical depth. These preliminary results suggest that BA played a key role in the graphitization process, probably acting as temperature regulator during laser writing, by reducing thermal degradation and ablation and facilitating graphitization.[34] Specifically, it is known that CS-BA composites show thermal stability, due to the formation of cross-linked, gel-like structures, a process that releases water preventing ablation during laser irradiation.[34] The presence of BA might also contribute to the observed expanded LIG morphology through the release of B_2O_3 gases during laser irradiation.

https://doi.org/10.1021/acsaelm.5c00234
ACS Appl. Electron. Mater. 2025, 7, 4801−4813

Table 1. High-Resolution XPS Fit Results for CS-LIGN-BA and LIG

		CS-LIGN-BA			LIG		
element(s)	peak assignment	position	%	fwhm	position	%	fwhm
carbon 1s	C═C	284.60	13.24	0.75	284.69	17.00	0.59
	C−C	284.96	18.96	1.00	285.31	14.47	0.89
	C−O	286.32	32.55	1.18	286.67	35.48	1.74
	C═O	288.08	4.88	1.03	288.49	3.23	2.55
boron 1s	B−N/B-O	191.83	1.27	1.02	193.17	2.97	1.49

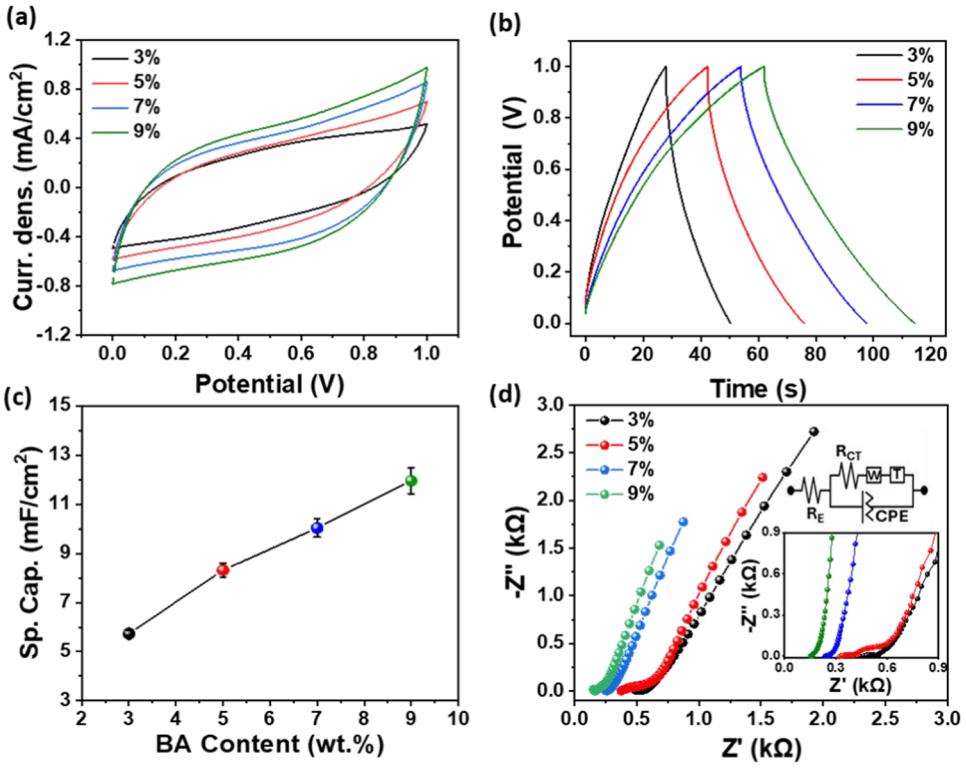

Figure 5. Electrochemical performance of LIG supercapacitors fabricated using CS-LIGN-BA substrates with varying BA content (wt %). (a) *CV* at a scan rate of 100 mV/s; (b) galvanostatic charge−discharge (GCD) curves; (c) specific areal capacitances for different BA contents at a current density of 0.2 mA/cm^2; (d) EIS Nyquist fitting plot of SC devices made of LIG with varying BA content (%) (inset: equivalent EIS circuit and high-frequency region of EIS).

Further characterization of LIG was performed by using Raman spectroscopy. Figure 4a shows a representative Raman spectrum of LIG obtained by laser writing of the CS-LIGN-BA substrate displaying three major peaks, typical of graphene-like carbon morphology. Specifically, the spectrum showed a D-band, related to bent sp^2 carbon and associated with defects, centered at 1351 cm^{-1}, a G-band centered at 1584 cm^{-1}, corresponding to the E_{2g} tangential vibrations of graphitic carbon, and a 2D-band related to second-order zone boundary phonons at 2698 cm^{-1} indicating conversion from amorphous carbon to crystalline graphitic carbon.[25] All the bands could be fitted by a single Lorentzian peak and showed full width at half max (fwhm) of 60.7, 34.7, and 73.2 cm^{-1} for the D, G, and 2D bands, respectively.[27] The Raman data showed that the quality of the herein produced LIG material had comparable characteristics with those of other LIG materials produced previously by our group and others using polyimide and other sustainable materials.[35−38] Specifically, the I_D/I_G ratio of 0.6 indicates formation of structures with significant degree of crystallinity within a disordered graphitic carbon network, whereas the I_{2D}/I_G ratio of 0.84, alongside a sharp 2D peak, highlights the formation of a graphene-like multilayer structure characterized by abundant defects and edges.[37] Figure 4b shows the XRD pattern of LIG, featuring a sharp major peak at 2θ = 27°, corresponding to the (002) graphitic crystal planes with an interlayer spacing of ∼0.34 nm, and a minor peak at 2θ = 53°, attributed to the (100) graphitic crystal phase. These data are in line with XRD patterns reported for other LIG structures obtained by laser writing of polyimide, paper, and biopolymers.[38] The thermal stabilization effect of BA in the CS-LIGN formulation was assessed by using thermogravimetric analysis (TGA). Figure 4c shows the thermal stability of CS-LIGN-BA compared with CS-LIGN substrates. For both materials, the TGA curves revealed distinct weight loss stages, highlighting the thermal stability differences between CS-LIGN and CS-LIGN-BA substrates. These stages were better visualized in the corresponding peaks of the DTA curves, shown as the inset in Figure 4c. For both materials, weight loss occurred in three stages: the first stage (Td_1), up to 100 °C corresponds to the desorption of physiosorbed water; the second stage (Td_2), extending to ca. 200 °C, was attributed to the loss of chemisorbed water; the third stage (Td_3) below 400

https://doi.org/10.1021/acsaelm.5c00234
ACS Appl. Electron. Mater. 2025, 7, 4801−4813

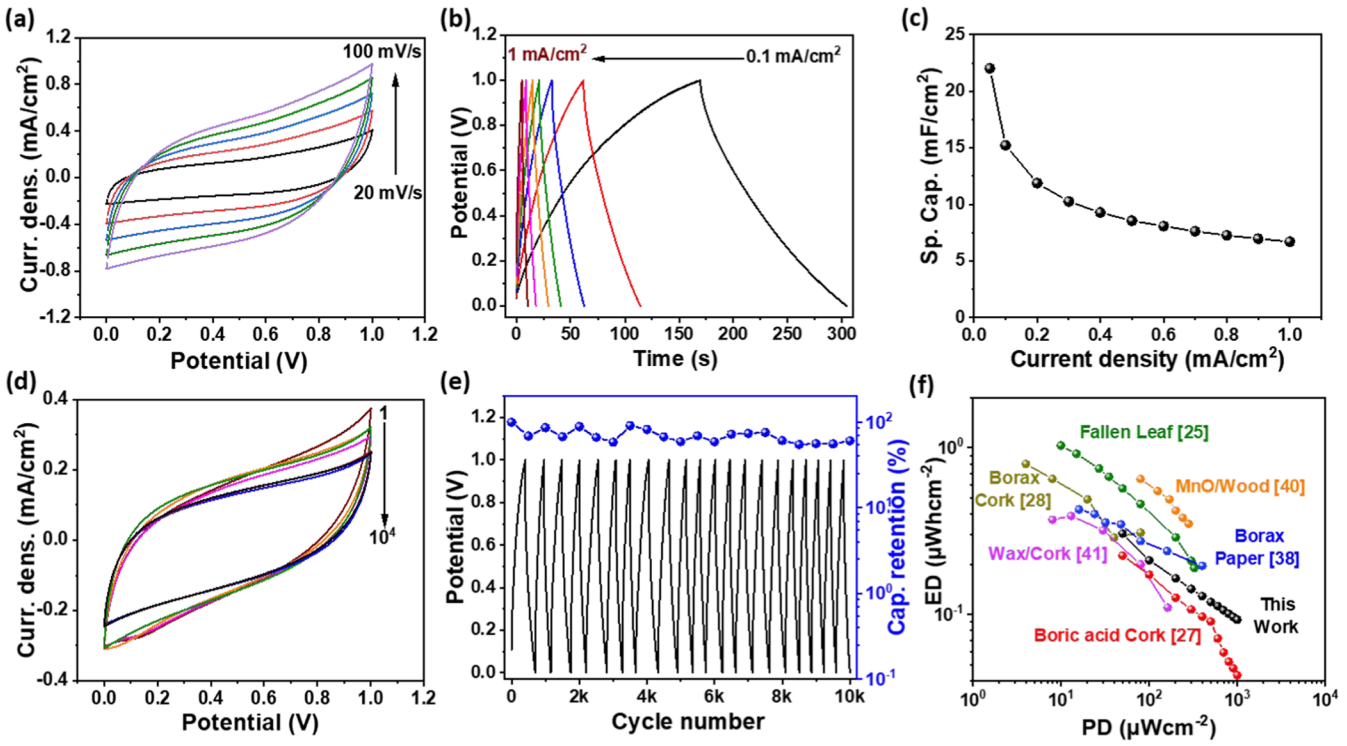

Figure 6. (a) *CV*s of LIG supercapacitors fabricated using CS-LIGN-BA substrates with 9 wt % BA content at different scan rates; (b) GCD curves; (c) Specific areal capacitances at different current densities; (d) selected *CV*s recorded during long-term cycling; (e) capacity retention recorded at regular intervals of 500 cycles up to 10,000 cycles; (f) Ragone plot comparing the supercapacitive performance with reported sustainable material-based electrodes.

°C, represents the thermal decomposition of CS and LIGN. The TGA profile for CS-LIGN showed a moisture weight loss of 25% at 63 °C and 67% at 161 °C, followed by a 68% weight loss at 268 °C due to CS decomposition through pyrolysis of the polysaccharide moiety, starting from a random split of the glycosidic bonds, followed by a further decomposition forming predominantly carboxylic acids.[39] In contrast, CS-LIGN-BA substrates displayed water loss of 63% at 53 °C and 81% at 187 °C, with a subsequent 9% loss at 359 °C. These results suggest that BA introduced a distinct mechanism for water loss in CS-LIGN-BA, attributed to its increased water content, arising from the neutralization reaction between boric acid and chitosan.[34] This could be responsible for the higher water loss observed in CS-LIGN-BA compared to CS-LIG and the higher temperature at which decomposition occurred (Td_3 of 359 °C for CS-LIGN-BA, 91 °C higher than the Td_3 of CS-LIGN). This observation aligns with earlier findings on LIG formation in CS-BA films, where the presence of BA, due to its radiation shielding capability, was found effective in enhancing the thermal stability of CS, supporting its efficient graphitization.[34] The obtained LIG structure was characterized by XPS to further evaluate the effect of BA on the graphitization process. Figure 4d,e shows the deconvoluted C 1s XPS peaks for pristine CS-LIGN-BA and LIG, respectively. The peaks were analyzed into four components, the main C═C sp^2 and C−C sp^3 carbon bonds, C−O(H) epoxides, hydroxides, and C═O carbonyl groups. Peak assignments and percentages of each component concentrations are shown in Table 1. XPS data indicated an increase in sp^2 carbon concentration from 13.24% in pristine CS-LIGN-BA to 17.0% in LIG, alongside a decrease in sp^3 carbon concentration from 18.96% to 14.47%, confirming the occurrence of graphitization.

Figure 4f shows the XPS boron peak for both CS-LIGN-BA and LIG-CS-LIGN-BA films. In the CS-LIGN-BA film, the boron peak appeared at 191.8 eV, corresponding to an atomic percentage of 1.27%, and was associated with the presence of B−O bonds. After laser irradiation, the boron peak shifted to a higher binding energy of 193.2 eV, indicative of B−O bond formation, and its atomic percentage increased to 2.97%, indicating the incorporation of BA into the LIG structure. The XPS spectrum of O 1s species (Figure S2a) showed a decrease in the overall oxygen content in LIG compared to the pristine CS-LIGN-BA substrate (Table S2), in line with results obtained for other LIG structures.

Supercapacitor Devices. Direct laser scribing was performed to produce LIG square patterns on CS-LIGN-BA films deposited on PET substrates. A sandwiched SC was fabricated by placing PVA/H^+ gel electrolyte (~80 μL) with a polypropylene separator (100 μm) between two LIG square electrodes. Then, the assembled SCs were connected to a potentiostat for electrochemical characterization. First, the electrochemical performances of SC devices assembled with LIG electrodes fabricated from CS-LIGN-BA substrates with different BA contents (3−9 wt %) were investigated. Figure 5a shows the cyclic voltammograms (*CV*) obtained for SCs with different percentages of BA, measured at a 100 mV/s scan rate. For all BA percentages, almost rectangular *CV* curves were obtained, indicating good electrochemical double-layer properties of the SCs and an increase in capacitive area as the percentage of BA increased. This trend was also evident from the almost triangularly shaped GCD curves recorded at a current rate of 0.2 mA/cm² (Figure 5b), showing larger discharge times for higher BA percentages. Accordingly, higher specific areal capacitances and longer discharge times were

https://doi.org/10.1021/acsaelm.5c00234
ACS Appl. Electron. Mater. 2025, 7, 4801−4813

measured for SC devices with higher BA percentages (Figure 5c). EIS was performed to evaluate the resistive nature of assembled SCs using LIG electrodes obtained from CS-LIGN-BA substrates (Figure 5d). The low frequency region of the Nyquist plot of the fitted EIS data showed a decrease in both internal and external resistances resulting from electrode−electrolyte interface as the BA content increased, whereas the high-frequency region showed an increase in semicircle with increase in BA content up-to a certain level after which the supercapacitive performance was not significantly influenced (see inset of Figure 5d). The plot showed a gradual reduction in equivalent series resistance (R_E) as the BA content (wt %) increased. During discharge processes, the initial IR drop values decreased from 55 to 26 mV with the increase of BA percentage from 3 to 9%, indicating a decreased internal resistance of the SC devices (Table S3).

Electrochemical characterization of SCs fabricated with LIG from CS-LIGN-BA (9%) was conducted to evaluate their capacitive behavior. Cyclic voltammetry analysis provided key insights into the charge storage mechanisms, allowing differentiation between diffusion-controlled pseudocapacitance (PC) and capacitive EDLC contributions (Figure S3a). *CV* curves recorded at different scan rates (20−100 mV/s) exhibited pseudorectangular shapes (Figure 6a), indicating good electric double-layer capacitive (EDLC) properties. GCD measurements at different charge−discharge rates from 0.1 to 1.0 mA/cm^2 showed pseudotriangular shapes, also indicating good capacitive properties (Figure 6b). The *CV* curve at a low scan rate of 10 mV/s and GCD curve at a low current density of 0.05 mA/cm^2 are presented in the SI (Figure S3b,c), demonstrating the capability of supercapacitive performance at a low scan rate and low current density. Specific areal capacitances for the SCs, calculated across various charge−discharge rates, showed a reduction in capacitance values with increasing discharge current density (Figure 6c). The SCs demonstrated impressive performance, retaining a capacitance of approximately 6.7 mF/cm^2 even when the discharge rate was increased 20-fold, from 0.05 to 1.0 mA/cm^2. A representative SC was cycled for over 10,000 cycles through continuous charge−discharge cycling to assess the long-term stability and performance. *CV* curves at a scan rate of 50 mV/s were recorded every 500 cycles (Figure 6d), and GCD curves were obtained at a charge−discharge rate of 1.0 mA/cm^2 (Figure 6e). SCs showed nearly stable capacitance retention, maintaining over 68% of their initial capacitance after 10,000 cycles. Close observation revealed that during the initial GCD cycling, the specific areal capacitance slightly increased before reaching stability, followed by a gradual decrease with further cycling. The initial increase in capacitance could be due to better penetration of the PVA/H$^+$ electrolyte into the porous LIG electrodes, resulting in higher ion transport and electrical double-layer formation between anodic and cathodic surfaces. To quantify the supercapacitive performance of the SCs, specific areal energy densities (ED) were calculated at various power densities (PD) based on the total geometric area of anode and cathode surfaces and displayed in a Ragone plot (Figure 6f) along with recent reported results obtained for supercapacitors based on LIG from sustainable sources. Specific gravimetric capacitances at different current rates (Figure S3d) showing capacitance up to 1.84 F/g were obtained at a 0.02 A/g current rate based on the total mass loading of dry CS-LIGN-BA film on the PET substrate (21.36 mg/cm^2). The impressive performance and long cycle stability of these LIG-biopolymer film-based SCs highlight the potential of chitosan as a viable energy storage material for sustainable electronics.

To evaluate their practical applicability, two SCs were connected in series and analyzed. This configuration was tested through cyclic voltammetry (*CV*) measurements at a scan rate of 100 mV/s (Figure S4a) and galvanostatic charge−discharge (GCD) curves at current densities of 0.2 and 0.3 mA/cm^2 (Figure S4b,c). The results confirmed the feasibility of achieving a higher voltage output by connecting multiple units of supercapacitors in series. Furthermore, to assess the capabilities for practical applications, SCs were charged with a commercial solar cell and used to power different devices, as shown in Figure 7. It was observed that SCs were instantly fully

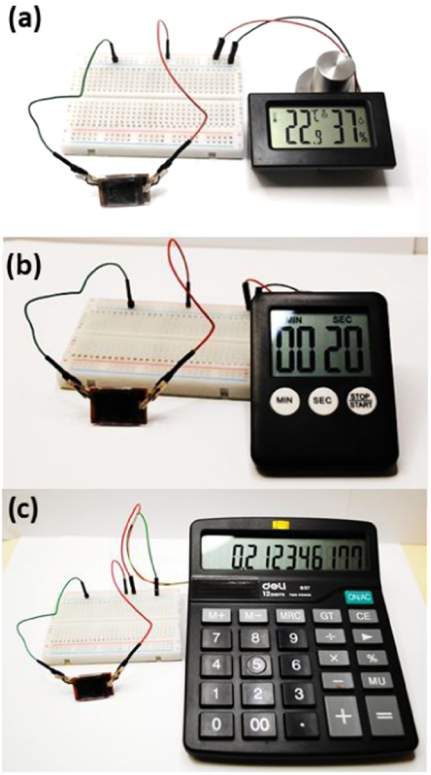

Figure 7. Photographs of a single LIG SC powering (a) a digital thermo-hygrometer; (b) an electronic stopwatch; and (c) a calculator.

charged by the solar cell, and once disconnected from the charging source, they were able to power a digital thermo-hygrometer, an electronic stopwatch, and a calculator.

Table 2 reports the comparison of the performance of the SC presented in this work with other "green" SCs fabricated by laser writing technologies. The LIG SCs were characterized by high specific capacitance and areal power density. The reported 68% capacity retention after 10,000 cycles was lower than other reported stability values. Our *CV* analysis indicated that charge storage occurred through a combination of EDLC and PC processes. The faradaic reactions associated with PC contributions may contribute to gradual electrode degradation, resulting in performance fading over prolonged cycling. Potential degradation mechanisms include electrolyte decomposition or drying over extended charge−discharge cycles, as well as structural instability of the biobased electrode material due to swelling, dissolution, or mechanical stress.[43−45]

https://doi.org/10.1021/acsaelm.5c00234
ACS Appl. Electron. Mater. 2025, 7, 4801−4813

Table 2. Comparison of Sustainable Material-Based LIGs for Supercapacitor Devices Reported in the Recent Literature

substrate materials	laser type/ wavelength	specific capacitance @ current density	areal power density	areal energy density	cyclic stability with capacity retention (%)	refs
Nageia fleuryi leaf	femtosecond laser	34.68 mF/cm^2 @ 5 mV/s	10 μW/cm^2	1.03 μWh/cm^2	50,000 (99%) @ 100 mV/s	25
boric acid-treated cork	450 nm	3.77−11.24 mF/cm^2 @ 0.1 mA/cm^2	55.7 μW/cm^2	1.7 μWh/cm^2	>10,000 (86%) @ 1 mA/cm^2	27
borax-treated cork	CO_2 laser	7−10 mF/cm^2 @ 0.01 mA/cm^2	4 μW/cm^2	≈0.77 μWh/cm^2	5000 (80−85%) @ 0.08 mA/cm^2	28
borax-treated paper	CO_2 laser	4.6 mF/cm^2 @ 0.015 mA/cm^2	0.3 μW/cm^2	4.5 μWh/cm^2	10,000 (85%) @ 0.5 mA/cm^2	38
MnO-embedded wood	femtosecond laser	35.54 mF/cm^2 @10 mV/s	0.67 μW/cm^2	80 μWh/cm^2	10,000 (82.31%) @100 mV/s	40
wax-treated agglomerated cork	Nd:YAG fiber laser	1.43 mF/cm^2 @0.1 mA/cm^2	8 μW/cm^2	0.37 μWh/cm^2	>10,000 (106%) @ 0.05 mA/cm^2	41
cotton cloth/MnO_2	Nd:YAG laser	54.97 mF/cm^2 @ 0.05 mA/cm^2	7.63 μW/cm^2	78.93 μWh/cm^2	10,000 (80.6%) @ 500 mV/s	42
CS-LIGN-BA	450 nm	21.4 mF/cm^2 @ 0.05 mA/cm^2	50 μW/cm^2	0.30 μWh/cm^2	>10,000 (68%) @ 1.0 mA/cm^2	this work

SE-TENG Devices. Figure 8a shows the schematic design of the SE-TENG device, comprising an LIG electrode obtained from direct laser writing of CS-LIGN-BA (9%) films on PET, a PDMS dielectric active layer, and PET as the counterpart material. Figure 8b illustrates the working principle of the single-electrode triboelectric nanogenerator (SE-TENG) operating in vertical contact-separation mode. In its initial state (i), the device exhibits no charge transfer or potential difference between its triboelectric layers. However, upon contact with the active surface of the SE-TENG, the counter material (PET) induces charge separation, due to differences in triboelectric affinities. Specifically, PDMS, which has a stronger tendency to attract electrons, gains a negative charge, while PET becomes positively charged, forming an oppositely charged interface. As the separation process begin (ii), the distance between the triboelectric layers increases, leading to an electrostatic potential difference. This potential imbalance drives electrons through the external circuit, generating a transient current flow until an equilibrium state is established (iii). Upon recontact (iv), mechanical force reduces the gap between the layers, leading to electron backflow in the opposite direction to restore charge equilibrium. This periodic contact and separation cycle results in a continuous alternating current (AC) output.

Prior to undertaking experimental work, a COMSOL Multiphysics simulation was performed to evaluate the suitability of PDMS as a triboelectric active layer utilizing the experimental parameters provided in Table S4. This included numerical calculations to demonstrate the higher surface electric potential of PDMS-LIG-SE-TENG compared to bare LIG-SE-TENG devices (Figure S5a,b), due to the inhibition of surface charge accumulation induced by the bare conductive LIG network. After confirmation of the suitability of PDMS as a dielectric layer material, the energy harvesting capability and functional stability of the assembled SE-TENG device were evaluated.

The electrical output performance of the device was first measured in terms of open-circuit potential (V_{OC}) over extended operating cycles at a frequency of 2 Hz, under varying drive forces of 30, 40, 50, and 60 N. To derive reliable conclusions about the performance of these devices, it is crucial to evaluate the V_{OC} behavior under different mechanical forces. In our study, the applied force during the activation of the nanogenerators exhibited an excellent linear positive correlation with V_{OC} increasing proportionally to the applied mechanical tension. Figure 8c shows the peak-to-peak V_{OC} outputs generated from the contact-separation processes for an SE-TENG device under forces between 30 and 60 N, showing the highest V_{OC} output of 25.8 V/cm^2. The data show a progressive increase of V_{OC}, associated with the increase of charge transfer produced by the greater interfacial contact area generated by the materials' plastic deformation under higher applied forces. In comparison, SE-TENG devices fabricated with no PDMS layer (using air as dielectric) showed a much lower performance, with V_{OC} outputs of 11.2 V/cm^2 (Figure S6). Figure 8d shows a significant increase in V_{OC} with an increasing frequency, reaching a plateau at approximately 8 Hz. Beyond this point, V_{OC} remained practically unchanged. This behavior is associated with the decrease of charge generation rate with the increase of trigger frequency. In systems with capacitive effects, lower frequencies allow sufficient time for charge accumulation, enabling the capacitor (or an equivalent charge storage mechanism) to fully charge during each cycle. However, once the frequency exceeds a certain threshold, the system reaches a saturation limit, where charge collection and transfer become inefficient due to material and circuit constraints. At high frequencies, the recombination rate of charge carriers may begin to match the generation rate, thereby limiting any further increase in V_{OC}. Furthermore, capacitive effects contribute to the saturation behavior, as the voltage across a capacitor requires time to build up and discharge. Additionally, at elevated frequencies, impedance variations within the circuit may further restrict the system's ability to sustain higher V_{OC} values. Once the system reaches its maximum charge transfer efficiency, further increases in frequency do not contribute to a higher V_{OC}, ultimately resulting in a steady-state response. Figure 8e shows the short-circuit current (I_{SC}), measured at 2 Hz, generated during the contact-separating cycling process and measured simultaneously with V_{OC} measurements. The I_{SC} values displayed an increase from 1.88 to 5.36 μA with an increase of contact-separation forces from 30 to 60 N. For I_{SC}, the TENG device exhibited performance with a trend like the V_{OC} trend, providing overall stable current outputs over the range of applied contact forces. The average I_{SC} values were measured as 0.24 ± 0.09 μA at a load resistance of 100 kΩ, increasing significantly to 5.57 ± 2.27 μA at 200 kΩ (Figure S7). The internal resistance and maximum peak power density of the TENG were measured by incorporating a series of variable load resistors into the external circuit. Figure 8f illustrates the

https://doi.org/10.1021/acsaelm.5c00234
ACS Appl. Electron. Mater. 2025, 7, 4801−4813

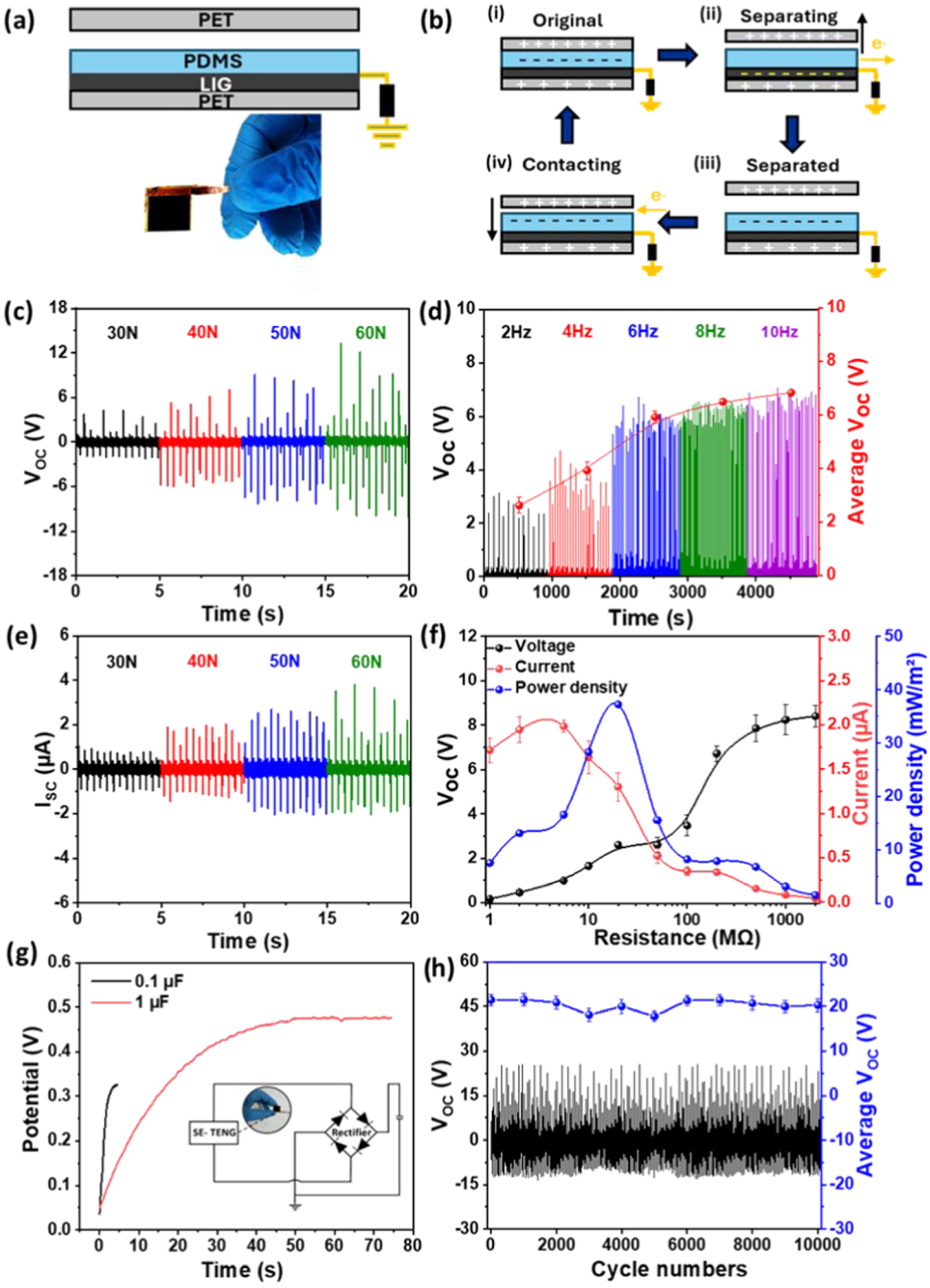

Figure 8. (a) Schematic of the SE-TENG device, composed of PDMS/LIG and (b) an illustration of its working principle in the single-electrode vertical contact-separation mode at various stages. (c) Open-circuit voltage (V_{OC}) peaks under different contact-separation forces. (d) Open-circuit voltage (V_{OC}) peaks under different operational frequencies. (e) Short-circuit current (I_{SC}) peaks under different contact-separation forces at 2 Hz. (f) Average V_{OC} and I_{SC} output values and peak power density (PD) across different external resistances. (g) Charging curves for 0.1 and 1 μF commercial capacitors (inset: operational circuit diagram). (h) Long-term stability of V_{OC} output.

TENG's power density behavior across the same range of load resistances. As the external load resistance varied from 0.1 to 200 MΩ, the V_{OC} increased from 0.17 to 8.4 V, while the peak current decreased from 1.7 to 0.042 μA. Furthermore, the I_{SC} exhibited a decline at higher external resistances, whereas the voltage across the load followed an inverse trend, increasing with resistance. Consequently, the power density generated by the TENG initially increased in the low-resistance region, reaching a maximum peak power of 8.9 mW/m^2 at a load resistance of 2 MΩ. This peak power corresponds to the resonant point where the external resistance aligns with the internal resistance of the TENG system, while beyond this point, the power density decreases in the high-resistance domain. To assess the TENG's energy storage capabilities, the TENG's alternating current (AC) output was converted into direct current (DC) utilizing a bridge rectifier consisting of four Schottky diodes for charging 0.1 and 1 μF commercial ceramic capacitors (Figure 8g with the circuit diagram depicted in inset). The load curves exhibited a swift rise in output voltage, leading to saturation of the capacitor. Notably, 0.1 μF capacitors demonstrated rapid charging, while the 1 μF capacitor required approximately 60 s to reach full charge.

https://doi.org/10.1021/acsaelm.5c00234
ACS Appl. Electron. Mater. 2025, 7, 4801−4813

Finally, the output stability was assessed by measuring the V_{OC} activated at 50 N, which showed minimal fluctuation in the average V_{OC} value and no decrease over 10,000 cycles (Figure 8h).

Finally, a comparative literature analysis with other SE-TENGs employing LIG as an electrode is presented in Table 3.

Table 3. Comparison of Power Density of LIG-Based SE-TENG for Energy Harvesting Reported in the Recent Literature[a]

active layer/ counterpart	electrodes	peak power density (mW/m^2)	references
PI/Al	PI-LIG	2.4	17
LF-LIG/PMMA	PI-LIG	512	46
SF-LIG/PMMA	PI-LIG	98	46
LIG/PMMA	PI-LIG	3.9	46
PDMS/Leaf	PI-LIG	80.8	47
PDMS/Au-LIG	PI-LIG/Au	11.1	48
CMCS/Acrylic	CS-LIG	2.48	36
CMCS/PI	CS-LIG	1.44	36
PDMS/LIG	CS-LIGN-BA-LIG	8.9	This work

[a]PMMA: poly(methyl methacrylate). SF-LIG: short carbon fiber combined LIG. LF-LIG: long carbon fiber dominant LIG. CMCS: carboxymethyl chitosan. PI: polyimide.

The observed peak power density surpassed many of the values reported in several recent publications, as summarized in the figure of merits. Interestingly, when evaluating TENGs with similar characteristics, such as those using LIG fabricated from CS and employing PDMS as an active layer, our device notably outperformed its counterparts by up to 335%. This significant result, coupled with the sustained stability demonstrated by the LIG-produced device, emphasizes the critical role of electrode optimization in achieving TENG's enhanced performance.

CONCLUSIONS

In this work, we have successfully explored the application of chitosan-based green, sustainable, and biodegradable materials as feedstock materials for the direct laser writing fabrication of LIG electrodes and their application in energy storage and harvesting devices. A simple one-step laser writing fabrication was enabled by the addition of BA to the initial feedstock formulation, which enhanced the heat resistance, thus preventing ablation and promoting graphitization. The fabricated SCs could successfully power LEDs and small electronic devices, such as a chronometer and an electronic calculator. The capacitive properties of the obtained LIG SC device showed improved performance with the increase of the BA content in the polymer matrix, leading to a final capacitance of 21.4 mF/cm^2 at a current rate of 0.05 mA/cm^2. An SE-TENG device was also fabricated using PDMS as a dielectric layer. The device showed a max V_{OC} of 13.3 V at 60 N and 2 Hz. The V_{OC} was also higher compared to other devices fabricated using LIG and PDMS. Considering the eco-friendly chemical composition of the feedstock material and the ease of LIG fabrication, and the performance of fabricated devices, direct laser writing of CS-LIGN-BA films is an attractive tool for the sustainable fabrication of future integrated energy storage/harvesting devices.

ASSOCIATED CONTENT

Supporting Information

The Supporting Information is available free of charge at https://pubs.acs.org/doi/10.1021/acsaelm.5c00234.

CS-LIGN-BA substrate compositions; SEM and EDS analysis; XPS spectra and data; supercapacitor electrochemical performance including IR drop, resistance, PC and EDLC contributions; series-connected SC analysis; and SE-TENG structural parameters, simulation results, and output voltage/current characteristics (PDF)

AUTHOR INFORMATION

Corresponding Authors

Luiz Henrique Capparelli Mattoso − *National Nanotechnology Laboratory for Agribusiness, Embrapa Instrumentação, São Carlos, SP 13560-970, Brazil;* orcid.org/0000-0001-7586-1014; Email: luiz.mattoso@embrapa.br

Daniela Iacopino − *Tyndall National Institute, University College Cork, Cork T12 R5CP, Ireland;* orcid.org/0000-0003-2301-9401; Email: daniela.iacopino@tyndall.ie

Authors

Jahidul Islam − *Tyndall National Institute, University College Cork, Cork T12 R5CP, Ireland*

Rafael Resende Assis Silva − *Graduate Program in Materials Science and Engineering (PPGCEM), Federal University of São Carlos (UFSCar), São Carlos, SP 13565-905, Brazil; CENIMAT/i3N, Department of Materials Science, NOVA School of Science and Technology, NOVA University Lisbon (FCT-NOVA) and CEMOP/UNINOVA, Caparica 2829-516, Portugal; National Nanotechnology Laboratory for Agribusiness, Embrapa Instrumentação, São Carlos, SP 13560-970, Brazil;* orcid.org/0000-0001-6112-8727

Alessandra Imbrogno − *Tyndall National Institute, University College Cork, Cork T12 R5CP, Ireland*

Caio G. Otoni − *Graduate Program in Materials Science and Engineering (PPGCEM), Federal University of São Carlos (UFSCar), São Carlos, SP 13565-905, Brazil; Institute of Chemistry, University of Campinas (UNICAMP), Campinas, SP 13083-970, Brazil;* orcid.org/0000-0001-6734-7381

Rodrigo Martins − *CENIMAT/i3N, Department of Materials Science, NOVA School of Science and Technology, NOVA University Lisbon (FCT-NOVA) and CEMOP/UNINOVA, Caparica 2829-516, Portugal*

Aidan J. Quinn − *Tyndall National Institute, University College Cork, Cork T12 R5CP, Ireland;* orcid.org/0000-0003-4021-9990

Complete contact information is available at: https://pubs.acs.org/10.1021/acsaelm.5c00234

Author Contributions

#J.I. and R.R.A.S. contributed equally to the work. J.I.: conceptualization, formal analysis, validation, writing—original draft; R.R.A.S.: conceptualization, formal analysis, validation, writing—original draft; A.I.: data curation; writing—review and editing; C.G.O.: funding acquisition, writing—review and editing; R.M.: supervision, funding acquisition, writing—review and editing; L.H.C.M.: supervision, writing—review and editing; A.J.Q.: supervision, writing—review and editing; D.I.: supervision, writing—review and editing, funding acquisition.

https://doi.org/10.1021/acsaelm.5c00234
ACS Appl. Electron. Mater. 2025, 7, 4801−4813

Funding

The Article Processing Charge for the publication of this research was funded by the Coordenacao de Aperfeicoamento de Pessoal de Nivel Superior (CAPES), Brazil (ROR identifier: 00x0ma614).

Notes

The authors declare no competing financial interest.

■ ACKNOWLEDGMENTS

This work has emanated from research conducted with the financial support of Research Ireland (RE), the Department of Agriculture, Food and Marine, on behalf of the Government of Ireland under Grant Number 16/RC/3835 (VISTAMILK). This work was supported by CNPq (Financing Code 200337/2022-0) and grant no. 406925/2022-4—INCT Circularity in Polymer Materials, CAPES (Financing Code 001), and FAPESP (grant no. 2021/12071-6). C.G.O. acknowledges CNPq (grant no. 304753/2022-0).

■ REFERENCES

(1) Kim, J.; Campbell, A. S.; de Ávila, B. E. F.; Wang, J. Wearable biosensors for healthcare monitoring. *Nat. Biotechnol.* **2019**, *37* (4), 389−406.
(2) Smith, A. A.; Li, R.; Tse, Z. T. H. Reshaping healthcare with wearable biosensors. *Sci. Rep.* **2023**, *13*, No. 4998.
(3) Seshadri, D. R.; Li, R. T.; Voos, J. E.; Rowbottom, J. R.; Alfes, C. M.; Zorman, C. A.; Drummond, C. K. Wearable sensors for monitoring the internal and external workload of the athlete. *NPJ. Digit. Med.* **2019**, *2*, No. 71.
(4) Kang, M.; Chai, K. Wearable sensing systems for monitoring mental health. *Sensors* **2022**, *22*, No. 994.
(5) Khoshmanesh, F.; Thurgood, P.; Pirogova, E.; Nahavandi, S.; Baratchi, S. Wearable sensors: At the frontier of personalised health monitoring, smart prosthetics and assistive technologies. *Biosens. Bioelectron.* **2021**, *176*, No. 112946.
(6) Yan, Z.; Luo, S.; Li, Q.; Wu, Z.; Liu, S. Recent advances in flexible wearable supercapacitors: Properties, fabrication, and applications. *Adv. Sci.* **2024**, *11*, No. 2302172.
(7) Pacchioni, G. Sustainable flexible supercapacitors. *Nat. Rev. Mater.* **2022**, *7*, No. 844.
(8) Bayoumy, A. M.; et al. Microdrop InkJet printed supercapacitors of graphene/graphene oxide ink for flexible electronics. *J. Power Sources* **2024**, *617*, No. 235145.
(9) Momeni, M. M.; Renani, A. S.; Lee, B. K. Light-chargeable two-electrode photo-supercapacitors based on MnS nanoflowers deposited on V2O5-BiVO4 photoelectrodes. *J. Alloys Compd.* **2023**, *962*, No. 171204.
(10) Xu, C.; Song, Y.; Han, M.; Zhang, H. Portable and wearable self-powered systems based on emerging energy harvesting technology. *Microsyst. Nanoeng.* **2021**, *7*, No. 25.
(11) Liu, R.; Wang, Z. L.; Fukuda, K.; Someya, T. Flexible self-charging power sources. *Nat. Rev. Mater.* **2022**, *7*, 870−886.
(12) Kaja, K. R.; Hajra, S.; Panda, S.; Belal, M. A.; Pharino, U.; Khanbareh, H.; Vittayakorn, N.; Vivekananthan, V.; Bowen, C.; Kim, H. J. Exploring liquid-solid interface based triboelectrification, structures, and applications. *Nano Energy* **2024**, *131*, No. 110319.
(13) Sahu, M.; Hajra, S.; Jadhav, S.; Panigrahi, B. K.; Dubal, D.; Kim, H. J. Bio-waste composites for cost-effective self-powered breathing patterns monitoring: An insight into energy harvesting and storage properties. *Sustain. Mater. Technol.* **2022**, *32*, No. e00396.
(14) Panda, S.; et al. Sustainable solutions for oral health monitoring: Biowaste-derived triboelectric nanogenerator. *Sustain.* **2019**, *11*, 1−14.
(15) Wang, Y.; Zhang, J.; Jia, X.; Chen, M.; Wang, H.; Ji, G.; Zhou, H.; Fang, Z.; Gao, Z. TENG-based self-powered device—the heart of life. *Nano Energy* **2024**, *119*, No. 109080.
(16) Babu, A.; Aazem, I.; Walden, R.; Bairagi, S.; Mulvihill, D. M.; Pillai, S. C. Electrospun nanofiber based TENGs for wearable electronics and self-powered sensing. *Chem. Eng. J.* **2023**, *452*, No. 139060.
(17) Ma, W.; Zhu, J.; Wang, Z.; Song, W.; Cao, G. Recent advances in preparation and application of laser-induced graphene in energy storage devices. *Mater. Today Energy* **2020**, *18*, No. 100569.
(18) Bai, S.; Ruan, L.; Chen, H.; Du, Y.; Tang, Y. Laser-induced graphene: Carbon precursors, fabrication mechanisms, material characteristics, and applications in energy storage. *Chem. Eng. J.* **2024**, *493*, No. 152805.
(19) Jo, S. G.; Ramkumar, R.; Lee, J. W. Recent advances in laser-induced graphene-based materials for energy storage and conversion. *ChemSusChem* **2024**, *17*, No. e202301146.
(20) Stanford, M. G.; Li, J. T.; Chyan, Y.; Wang, Z.; Wang, W.; Tour, J. M. Laser-induced graphene triboelectric nanogenerators. *ACS Nano* **2019**, *13*, 7166−7174.
(21) Yan, J.; Wang, H.; Wang, X.; Yang, G. High-performance triboelectric nanogenerators with laser-induced graphene pattern for efficient charge transfer. *Appl. Surf. Sci.* **2024**, *661*, No. 160034.
(22) Yang, W.; Han, M.; Liu, F.; Wang, D.; Gao, Y.; Wang, G.; Ding, X.; Luo, S. Structure-foldable and performance-tailorable PI paper-based triboelectric nanogenerators processed and controlled by laser-induced graphene. *Adv. Sci.* **2024**, *11*, No. 2310017.
(23) Shrestha, K.; Sharma, S.; Pradhan, G. B.; Lee, S. H.; Park, J. Y. A triboelectric driven rectification free self-charging supercapacitor for smart IoT applications. *Nano Energy* **2022**, *102*, No. 107713.
(24) Claro, P. I. C.; Pinheiro, T.; Silvestre, S. L.; Marques, A. C.; Coelho, J.; Marconcini, J. M.; Fortunato, E.; Mattoso, L. H. C.; Martins, R. Sustainable carbon sources for green laser-induced graphene: A perspective on fundamental principles, applications, and challenges. *Appl. Phys. Rev.* **2022**, *9*, No. 041305.
(25) Le, T. D.; et al. Green flexible graphene−inorganic-hybrid micro-supercapacitors made of fallen leaves enabled by ultrafast laser pulses. *Adv. Funct. Mater.* **2022**, *32*, No. 2107768.
(26) Larrigy, C.; Burke, M.; Imbrogno, A.; Vaughan, E.; Santillo, C.; Lavorgna, M.; Sygellou, L.; Paterakis, G.; Galiotis, C.; Iacopino, D.; Quinn, A. J. Porous 3D graphene from sustainable materials: Laser graphitization of chitosan. *Adv. Mater. Technol.* **2023**, *8*, No. 2201228.
(27) Imbrogno, A.; Islam, J.; Santillo, C.; Castaldo, R.; Sygellou, L.; Larrigy, C.; Murray, R.; Vaughan, E.; Hoque, M. K.; Quinn, A. J.; Iacopino, D. Laser-induced graphene supercapacitors by direct laser writing of cork natural substrates. *ACS Appl. Electron. Mater.* **2022**, *4*, 1541−1551.
(28) Silvestre, S. L.; Morais, M.; Soares, R. R. A.; Johnson, Z. T.; Benson, E.; Ainsley, E.; Pham, V.; Claussen, J. C.; Gomes, C. L.; Martins, R.; Fortunato, E.; Pereira, L.; Coelho, J. Green fabrication of stackable laser-induced graphene micro-supercapacitors under ambient conditions: Toward the design of truly sustainable technological platforms. *Adv. Mater. Technol.* **2024**, *9*, No. 2400261.
(29) Chi, Y.; Xia, K.; Zhu, Z.; Fu, J.; Zhang, H.; Du, C.; Xu, Z. Rice paper-based biodegradable triboelectric nanogenerator. *Microelectron. Eng.* **2019**, *216*, No. 111059.
(30) Saqib, Q. M.; Shaukat, R. A.; Khan, M. U.; Chougale, M.; Bae, J. Biowaste peanut shell powder-based triboelectric nanogenerator for biomechanical energy scavenging and sustainably powering electronic supplies. *ACS Appl. Electron. Mater.* **2020**, *2*, 3953−3963.
(31) Singh, H.; Sheetal, A.; Kaur, J.; Singh, M.; Sharma, M. Generation of electrical energy using fish market waste fish fin from mechanical motion for battery-less self-powered wearable sensors and IoT devices. *Electron. Mater. Lett.* **2023**, *19*, 483−494.
(32) Germane, L.; Lapčinskis, L.; Iesalnieks, M.; Šutka, A. Surface engineering of PDMS for improved triboelectrification. *Mater. Adv.* **2023**, *4*, 875−880.
(33) Peng, Z.; Ye, R.; Mann, J. A.; Zakhidov, D.; Li, Y.; Smalley, P. R.; Lin, J.; Tour, J. M. Flexible boron-doped laser-induced graphene microsupercapacitors. *ACS Nano* **2015**, *9*, 5868−5875.
(34) Vaughan, E.; Santillo, C.; Imbrogno, A.; Gentile, G.; Quinn, A. J.; Kaciulis, S.; Lavorgna, M.; Iacopino, D. Direct laser writing of

chitosan−borax composites: Toward sustainable electrochemical sensors. *ACS Sustain. Chem. Eng.* **2023**, *11*, 13574−13583.
(35) Vaughan, E.; Larrigy, C.; Burke, M.; Sygellou, L.; Quinn, A. J.; Galiotis, C.; Iacopino, D. Visible laser scribing fabrication of porous graphitic carbon electrodes: Morphologies, electrochemical properties, and applications as disposable sensor platforms. *ACS Appl. Electron. Mater.* **2020**, *2*, 3279−3288.
(36) Huang, Q. M.; Yang, H.; Wang, S.; Liu, X.; Tan, C.; Luo, A.; Xu, S.; Zhang, G.; Ye, H. Laser-induced graphene formation on chitosan derivatives toward ecofriendly electronics. *ACS Appl. Nano Mater.* **2023**, *6*, 10453−10465.
(37) Vaughan, E.; Santillo, C.; Setti, M.; Larrigy, C.; Quinn, A. J.; Gentile, G.; Lavorgna, M.; Iacopino, D. Sustainable laser-induced graphene electrochemical sensors from natural cork for sensitive tyrosine detection. *Adv. Sens. Res.* **2023**, *2*, No. 220026.
(38) Coelho, J.; Correia, R. F.; Silvestre, S.; Pinheiro, T.; Marques, A. C.; Correia, M. R. P.; Vaz Pinto, J.; Fortunato, E.; Martins, R. Paper-based laser-induced graphene for sustainable and flexible microsupercapacitor applications. *Microchim. Acta* **2023**, *190*, No. 40.
(39) Neto, C. G. T.; Giacometti, J. A.; Job, A. E.; Ferreira, F. C.; Fonseca, J. L. C.; Pereira, M. R. Thermal analysis of chitosan based networks. *Carbohydr. Polym.* **2005**, *62*, 97−103.
(40) Kim, Y.-R.; Nam, H.-K.; Lee, Y.; Yang, D.; Le, T.-S. D.; Kim, S.-W.; Park, S.; Kim, Y.-J. Green supercapacitor patterned by synthesizing MnO/laser-induced-graphene hetero-nanostructures on wood via femtosecond laser pulses. *Biochar* **2024**, *6*, No. 36.
(41) Silvestre, S. L.; Pinheiro, T.; Marques, A. C.; Deuermeier, J.; Coelho, J.; Martins, R.; Pereira, L.; Fortunato, E. Cork derived laser-induced graphene for sustainable green electronics. *Flex. Print. Electron.* **2022**, *7*, No. 035021.
(42) Lu, L.; Zhang, D.; Xie, Y.; Wang, W. A stretchable, high-voltage and biobased microsupercapacitor using laser induced graphene/MnOx electrodes on cotton cloth. *J. Energy Storage* **2022**, *51*, No. 104458.
(43) Khan, Z.; Singh, P.; Ansari, S. A.; Manippady, S. R.; Jaiswal, A.; Saxena, M. VO_2 nanostructures for batteries and supercapacitors: A review. *Small* **2021**, *17*, No. 2006651.
(44) Ali, G. A. M.; Ansari, S.; Manippady, S. R.; Jaiswal, A.; Saxena, M. Superior supercapacitance behavior of oxygen self-doped carbon nanospheres: A conversion of Allium cepa peel to energy storage system. *Biomass Convers. Biorefin.* **2021**, *11*, 1311−1323.
(45) Yamada, S. A transient supercapacitor with a water-dissolvable ionic gel for sustainable electronics. *ACS Appl. Mater. Interfaces* **2022**, *14*, 26595−26603.
(46) Choi, K.-H.; Park, S.; Hyeong, S.-K.; Bae, S.; Hong, J.-M.; Kim, T.-W.; Lee, S. H.; Ryu, S.; Lee, S. K. Triboelectric effect of surface morphology controlled laser induced graphene. *J. Mater. Chem. A* **2020**, *8*, 19822−19832.
(47) Li, X.; Jiang, C.; Zhao, F.; Shao, Y.; Ying, Y.; Ping, J. A self-charging device with bionic self-cleaning interface for energy harvesting. *Nano Energy* **2020**, *73*, No. 104738.
(48) Chen, H.; Yang, W.; Huang, P.; Li, C.; Yang, Y.; Zheng, B.; Zhang, C.; Liu, R.; Li, Y.; Xu, Y.; Wang, J.; Li, Z. A multiple laser-induced hybrid electrode for flexible triboelectric nanogenerators. *Sustain. Energy Fuels* **2021**, *5*, 3737−3743.

https://doi.org/10.1021/acsaelm.5c00234
ACS Appl. Electron. Mater. 2025, 7, 4801−4813